ELSEVIER

Crustal thickness of the Moon: New constraints from gravity inversions using polyhedral shape models

Hajime Hikida [a,*], Mark A. Wieczorek [b]

[a] *German Aerospace Center, Rutherfordstraße 2, D-12489 Berlin, Germany*
[b] *Institut de Physique du Globe de Paris, France*

Abstract

A new method is presented for estimating crustal thickness from gravity and topography data on the Moon. By calculating analytically the exterior gravitational field for a set of arbitrarily shaped polyhedra, relief along the crust–mantle interface can be inverted for that satisfies the observational constraints. As this method does not rely upon filtering the Bouguer anomaly, which was required with previous inversions performed in the spherical-harmonic domain, and as the dramatic variations in spatial quality of the lunar gravity field are taken into account, our crustal thickness model more faithfully represents the available data. Using our model results, we investigate various aspects of the prominent nearside impact basins. The crustal thickness in the central portion of the Orientale and Crisium basins is found to be close to zero, suggesting that these basins could have conceivably excavated into the lunar mantle. Furthermore, given our uncertain knowledge of the density of the crust and mantle, it is possible that the Humorum, Humboldtianum, Nectaris, and Smythii basins could have excavated all the way through the crust as well. The crustal structure for most of the young impact basins implies a depth/diameter ratio of about 0.08 for their excavation cavities. As noted in previous studies, however, the crustal structure of Imbrium and Serenitatis is anomalous, which is conceivably a result of enhanced rates of post-impact viscous relaxation caused by the proximity of these basins to the Procellarum KREEP Terrane. Impact basins older than Smythii show little or no evidence for crustal thinning, suggesting that these ancient basins were also affected by high rates of viscous relaxation resulting from higher crustal temperatures early in the Moon's evolution. The lithosphere beneath many young basins is found to be supporting a downward directed force, even after the load associated with the mare basalts is removed, and this is plausibly attributed to superisostatic uplift of the crust–mantle interface. Those basins that are close to achieving a pre-mare isostatic state are generally found to reside within, or close to, the Procellarum KREEP Terrane.

© 2007 Elsevier Inc. All rights reserved.

Keywords: Moon; Impact processes; Moon, interior

1. Introduction

Unlike the Earth, the Moon possesses near-pristine examples of large impact basins that formed during the first billion years of Solar System evolution. Basin-forming impacts are one of the major geologic processes that shaped the early landscape of the terrestrial planets (e.g., Melosh, 1989), and as such, the Moon is an ideal place for investigating the cratering process. For the Moon, relative variations in crustal thickness can be inferred from its observed gravitational field and topography, and the largest basins show evidence for significant crustal thinning (Phillips and Dvorak, 1981; Bratt et al., 1985; Neumann et al., 1996). The inferred crustal structure of these basins can be used to place constraints not only on various aspects of the basin forming process, but also on the thermal evolution of the Moon (Wieczorek and Phillips, 1999).

Since planets are nearly spherical bodies, their gravitational fields and topography are commonly expressed in spherical-harmonic functions. These global basis functions are analogous to the sines and cosines of a Cartesian Fourier series, and the relationship between gravity and topography is readily quantified in this domain (e.g., Wieczorek and Phillips, 1998). Nevertheless, the Moon suffers from a peculiar problem. While the

---

* Corresponding author. Fax: +49 30 67055 303.
  E-mail address: hikida.hikida@dlr.de (H. Hikida).

topography of this body is known globally with a relatively uniform spatial resolution (Smith et al., 1997; USGS, 2002; Archinal et al., 2006), the synchronous rotation of the Moon has precluded the radio tracking of spacecraft over large portions of the farside hemisphere. While the farside gravity field has been constrained by indirect means to a low precision (e.g., Konopliv et al., 2001), the spatial resolution of the nearside is considerably higher.

Previous investigations (e.g., Zuber et al., 1994; Neumann et al., 1996; Wieczorek and Phillips, 1998) have demonstrated that inversions for crustal thickness performed in the spherical-harmonic domain are unstable for the Moon as a result of the exponential increase of errors that occurs when the Bouguer anomaly is downward continued to the crust–mantle interface. To compensate for this, and to obtain reasonable solutions, this gravitational signature has been filtered (e.g., Phipps Morgan and Blackman, 1993). Filtering in the spherical-harmonic domain, however, does not take into account the dramatic lateral variations in quality of the lunar gravity data set. As one example, Wieczorek and Phillips (1998) applied a filter with a value of 0.5 at spherical-harmonic degree 30, whereas the resolution of the nearside gravity field can reach almost degree 150. Thus, in order to obtain of global solution in the spherical-harmonic domain, the global resolution was required to be close to the worst resolution of the gravity field, which is about degree 15 (see Konopliv et al., 2001).

To overcome this difficulty, we will invert for the crustal thickness of the Moon using a method developed in the spatial domain. In particular, we will employ the previously developed method of Werner and Scheeres (1997) for calculating analytically the exterior gravitational field of arbitrarily shaped constant-density polyhedra. For these computations we need to know only the location of each vertex of the polyhedra, and the radii of these are constrained either by the known surface topography or are inverted for at the crust–mantle interface in order to match the observed gravitational field. As benefits of this approach, the spatial resolution of the crustal thickness model can be easily tailored where necessary, and when inverting for the crust–mantle relief we can weight the misfit function by the uncertainties associated with the observed gravity field. In comparison to the spherical-harmonic inversions, however, the benefits associated with this method come at the expense of a considerable increase in computational burden.

In this paper we first describe how the gravitational field can be computed from a polyhedral shape model and how the relief along the crust–mantle interface can be inverted for utilizing the observed gravity and surface topography. Details concerning these calculations are presented in Appendixes A and B. Following this, we present our model results, describe how they depend upon various assumptions, and compare with inversions performed in the spherical-harmonic domain. Finally, we discuss the global features of our model, compare our predictions with the available seismic constraints, quantify the structure of the most prominent impact basins, and estimate the magnitude of the load the lithosphere is currently supporting beneath the basins.

2. Method

In this section we first describe the method by which we calculate the gravitational field of a body using arbitrarily shaped constant-density polyhedra. This is based on the work of Werner and Scheeres (1997), and while we give a brief sketch of the methodology here, the reader is referred to their paper for further details. Given a forward modeling procedure for obtaining the gravity field associated with a polyhedral shape model, we next describe how one can invert for the shape of a polyhedron given an external gravity field. We note that a spatial inversion for the thickness of the lunar crust has been performed both locally and globally by von Frese et al. (1997) and Potts and von Frese (2003a, 2003b), respectively. A major difference with their approach is that they only modeled gravitational signatures that were correlated with the surface topography.

2.1. Exterior gravitational field of a constant density polyhedron

By use of Gauss' divergence theorem, the gravitational potential external to a constant density object can be calculated either by an integral over its volume or surface:

$$V = G\rho \iiint\limits_V \frac{dV}{r'} = \frac{G\rho}{2} \iint\limits_S \frac{\hat{\boldsymbol{n}} \cdot \boldsymbol{r}'}{r'} \, dS, \tag{1}$$

where G is the gravitational constant, ρ is the density, $\boldsymbol{r}'$ is a vector from the observational point $\boldsymbol{r}$ to the differential volume or surface element, and $\hat{\boldsymbol{n}}$ is the unit-normal vector of the surface. If one assumes that the object can be approximated by a polyhedron, Werner and Scheeres (1997) have shown that the right-hand side of Eq. (1) can be converted into two sums, one over each of the edges of the polyhedron and the other over each of its faces:

$$V = \frac{G\rho}{2} \sum_{\text{edges}} \left\{ (\boldsymbol{r}_e \cdot \hat{\boldsymbol{n}}_A)(\hat{\boldsymbol{n}}_{12}^A \cdot \boldsymbol{r}_e) + (\boldsymbol{r}_e \cdot \hat{\boldsymbol{n}}_B)(\hat{\boldsymbol{n}}_{21}^B \cdot \boldsymbol{r}_e) \right\} L_e$$
$$- \frac{G\rho}{2} \sum_{\text{faces}} (\boldsymbol{r}_f \cdot \hat{\boldsymbol{n}}_f)^2 \omega_f. \tag{2}$$

Given this equation, it is straightforward to show that the gravitational acceleration (assumed to be positive when directed upwards) is given by

$$\boldsymbol{g} \equiv \nabla V$$
$$= G\rho \sum_{\text{edges}} \left\{ \hat{\boldsymbol{n}}_A (\hat{\boldsymbol{n}}_{12}^A \cdot \boldsymbol{r}_e) + \hat{\boldsymbol{n}}_B (\hat{\boldsymbol{n}}_{21}^B \cdot \boldsymbol{r}_e) \right\} L_e$$
$$- G\rho \sum_{\text{faces}} \hat{\boldsymbol{n}}_f (\hat{\boldsymbol{n}}_f \cdot \boldsymbol{r}_f) \omega_f. \tag{3}$$

Concerning the first sum in Eqs. (2) and (3), which is performed over all edges of the polyhedron, $\hat{\boldsymbol{n}}_A$ and $\hat{\boldsymbol{n}}_B$ are the unit-normal vectors of two faces that are connected by a single edge. If we define $\boldsymbol{r}_{12}$ as the vector pointing from vertex $\boldsymbol{r}_1$ to vertex $\boldsymbol{r}_2$ of this edge, then the unit vectors $\hat{\boldsymbol{n}}_{12}^A$ and $\hat{\boldsymbol{n}}_{21}^B$ are defined as

$$\hat{\boldsymbol{n}}_{12}^A = \hat{\boldsymbol{r}}_{12} \times \hat{\boldsymbol{n}}_A,$$

$$\hat{\boldsymbol{n}}_{21}^{B} = \hat{\boldsymbol{n}}_{B} \times \hat{\boldsymbol{r}}_{12}. \tag{4}$$

$\boldsymbol{r}_e$ is a vector from the observation point to any point on the line made by the two vertices $\boldsymbol{r}_1$ and $\boldsymbol{r}_2$, of which we choose $\boldsymbol{r}_1$ for this study. L_e is the function

$$L_e = \ln \frac{a+b+e}{a+b-e}, \tag{5}$$

where a and b are the distances from the observation point to vertex $\boldsymbol{r}_1$ and $\boldsymbol{r}_2$, respectively (i.e., $a = r_e$), and e is the edge length r_{12}.

The second summation in Eqs. (2) and (3) is performed over all faces of the polyhedron. Here, $\hat{\boldsymbol{n}}_f$ is the unit-normal vector of a given face, and $\boldsymbol{r}_f$ is a vector from the observation point to any point in the plane of this face. In this study, each face will be a triangular patch defined by three vertices $\boldsymbol{r}_1$, $\boldsymbol{r}_2$, and $\boldsymbol{r}_3$ ordered counterclockwise about the face normal $\hat{\boldsymbol{n}}_f$, and the vector $\boldsymbol{r}_f$ will be allocated to the vertex $\boldsymbol{r}_1$. Finally, ω_f is a solid angle associated with each face given by

$$\omega_f = 2 \arctan \frac{\beta}{\alpha}, \tag{6}$$

where

$$\begin{aligned} \alpha &= |\boldsymbol{r}_1 - \boldsymbol{r}||\boldsymbol{r}_2 - \boldsymbol{r}||\boldsymbol{r}_3 - \boldsymbol{r}| + |\boldsymbol{r}_1 - \boldsymbol{r}|(\boldsymbol{r}_2 - \boldsymbol{r}) \cdot (\boldsymbol{r}_3 - \boldsymbol{r}) \\ &\quad + |\boldsymbol{r}_2 - \boldsymbol{r}|(\boldsymbol{r}_3 - \boldsymbol{r}) \cdot (\boldsymbol{r}_1 - \boldsymbol{r}) \\ &\quad + |\boldsymbol{r}_3 - \boldsymbol{r}|(\boldsymbol{r}_1 - \boldsymbol{r}) \cdot (\boldsymbol{r}_2 - \boldsymbol{r}), \end{aligned} \tag{7}$$

$$\beta = (\boldsymbol{r}_1 - \boldsymbol{r}) \cdot (\boldsymbol{r}_2 - \boldsymbol{r}) \times (\boldsymbol{r}_3 - \boldsymbol{r}). \tag{8}$$

We note that both the numerator and denominator of the argument for the arctan function is signed and must be taken into account when computing this value. The reader is referred to Figs. 3, 5, 6, and 7 of Werner and Scheeres (1997) for a more complete description of the geometry and notation of the above vectors and quantities. We note that for a given polyhedron, all unit vectors in Eqs. (2) and (3) only needed to be computed once, whereas $\boldsymbol{r}_e$, L_e, $\boldsymbol{r}_f$, and ω_f need to be recomputed for each observation point.

2.2. Inversion strategy

The previous section described how one could calculate the gravitational field of a constant density body by approximating its shape in terms of a polyhedron. In this section, we will describe how one can conversely invert for the shape of a polyhedron given knowledge of the external gravity field. In particular, for our investigation of crustal thickness variations, we will assume that the structure of the Moon can be described by possessing a crust, mare basalts, mantle and core, all having constant densities (see Fig. 1). We will first calculate the gravitational field of a polyhedron with density ρ_{mare} that corresponds to the known shape of the Moon. Next, the gravitational attraction of a polyhedron with density $(\rho_{\text{mare}} - \rho_{\text{crust}})$ will be subtracted from this using the shape of the Moon with the thickness of the mare basalts removed. After adding the gravitational contribution of a small spherical core with a density
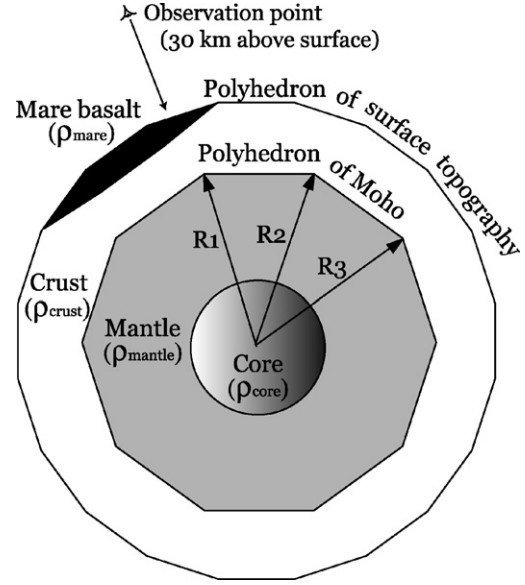

Fig. 1. Schematic illustration of our polyhedral shape model of the Moon. Each layer has a constant density and the vertical gravitational acceleration is calculated at an altitude of 30 km above the average surface radius.

$(\rho_{\text{core}} - \rho_{\text{mantle}})$, we will then invert for the shape of a polyhedron whose surface corresponds to the crust–mantle interface using a density $(\rho_{\text{mantle}} - \rho_{\text{crust}})$.

In this investigation, we model only the radial gravitational field of the Moon. Since we will sample the gravitational field derived from a spherical-harmonic model of the gravitational potential on a set of grid points (and not use direct line-of-sight observations), it is straightforward to show that the radial gravitational component contains all information of the spherical-harmonic model. Modeling the other two components would only introduce redundant constraints. In practice, the radial component of the gravity field will be calculated on a set of grid points on the surface of a sphere 30 km above the mean planetary radius, which corresponds to the average altitude of the Lunar Prospector spacecraft during its extended mission (see Konopliv et al., 2001).

In order to invert for the shape of the crust–mantle interface, it will be assumed that the densities of the crust, mare basalts, mantle, and core are known. Furthermore, we will assume a core radius, and use known models of the lunar shape, mare thickness, and gravitational field sampled on an appropriate grid (see Section 3). With these assumptions, the only unknowns that remain are the radii of the vertices that comprise the polyhedral model of the crust–mantle interface, $(r_1, r_2, \ldots, r_N)$. We define the misfit between the observed and calculated radial gravity, weighted by the uncertainty of the observed gravity σ, on a set of N grid points (θ_i, ϕ_i) as

$$f(r_1, r_2, \ldots, r_N) = \frac{1}{N} \sum_{i=1}^{N} \left(\frac{g_i^{\text{obs}} - g_i(r_1, r_2, \ldots, r_N)}{\sigma_i} \right)^2, \tag{9}$$

where

$$\begin{aligned} &g_i(r_1, r_2, \ldots, r_N) \\ &= g_i^{\text{topo}} + g_i^{\text{mare}} + g_i^{\text{mantle}}(r_1, r_2, \ldots, r_N) + g^{\text{core}}. \end{aligned} \tag{10}$$

All gravitational accelerations are calculated at the same radius of observation, R_{obs}.

The goal at this point is to find those radii of the mantle polyhedral model, $(r_1, r_2, \ldots, r_N)$, that minimize the misfit function Eq. (9). For this purpose, we use the Polak–Ribière conjugate gradient method (see Press et al., 1992, chap. 10), which is an efficient algorithm for finding the nearest local minimum of a multi-dimensional function. This method requires computation of the gradient of the misfit function, and uses conjugate directions instead of the local gradient in order to iteratively approach the minimum misfit. The components of the gradient matrix are given by

$$\frac{\partial f}{\partial r_j} = -\frac{2}{N} \sum_{i=1}^{N} \left(\frac{g_i^{\text{obs}} - g_i(r_1, r_2, \ldots, r_N)}{\sigma_i} \right) \frac{\partial g_i^{\text{mantle}}}{\partial r_j}, \qquad (11)$$

and analytic expressions for the partial derivatives of g_i^{mantle} are given in Appendix B. Given an initial estimate of the mantle shape, $(r_1, r_2, \ldots, r_N)$ are iteratively updated until convergence is achieved with condition $f \leqslant 1$.

The calculation of the partial derivatives of g_i^{mantle} can be somewhat time consuming, especially when the shape model contains thousands of points, as is the case here. In order to reduce the total computational time, we will compute only those terms where the angular distance between two vertices i and j is less than γ. The rationale for doing so is that the partial derivatives will naturally become smaller as the distance between two vertices i and j increases, and at some point the derivative will be negligible. While the descent path using the conjugate gradient method will not be optimal by discarding these terms, the dramatic decrease in computation time will allow us to perform many more iterations than would otherwise be possible. The exact choice of γ concerns primarily computation speed, and different values should all eventually reach the same solution if it is sufficiently large. Based on timing results, we have chosen a value of γ corresponding to 20 degrees.

Finally, we note that while we have calculated the shape model of the crust–mantle interface by minimizing the difference between the observed and calculated radial gravity, we could have equally chosen to have minimized the difference between their respective gravitational potentials. Tests using the potential function yielded very similar results, though minimization of the gravitational misfit function required fewer iterations, and thus less computer time.

3. Results

Before inverting the observed topography and gravity field of the Moon for a crustal thickness model, several parameters need to be specified (see Table 1). In particular, it is necessary to assume values for the density of the crust, mare basalts and mantle, as well as the core density and radius. Previous crustal thickness inversions for the Moon did not require information about the core (Zuber et al., 1994; Neumann et al., 1996; Wieczorek and Phillips, 1998) as only variations in the gravitational field with respect to a mean value were modeled. However, since our method calculates the absolute gravitational attraction, knowledge of the entire density structure of the Moon

Table 1
Parameters and properties of the polyhedral crustal thickness model

Parameter	Symbol	Value	Unit
GM	GM	4902.80295×10^9	$\text{m}^3\,\text{s}^{-2}$
Mean planetary radius	R	1737.1	km
Observational radius	R_{obs}	1767	km
Density of crust	ρ_{crust}	2800	kg m^{-3}
Density of mare basalts	ρ_{mare}	3100	kg m^{-3}
Density of mantle	ρ_{mantle}	3360	kg m^{-3}
Core radius	R_{core}	370	km
Density of core	ρ_{core}	6600	kg m^{-3}
Average crustal thickness	–	43	km
Minimum crustal thickness	–	<1	km
Maximum crustal thickness	–	85	km
Crustal thickness at A12/14	–	40	km

is required. As discussed below, presuming that the density of the crust and core are known, the core radius will directly determine the mantle density and average crustal thickness.

We use a value of 2800 kg m^{-3} for the density of the lunar crust, which is consistent with estimates based on the mineralogy of central peaks after considering a few percent porosity (see Wieczorek and Zuber, 2001; Wieczorek et al., 2006). As for the mare basalts, we have estimated the pore-free densities of the major mare basalt sample groupings by calculating mineralogical norms based on their major oxide compositions. Given the high iron content of the lunar basalts, their densities are relatively high in comparison to their terrestrial counterparts, with values between about 3100 and 3450 kg m^{-3}. After taking into account about 5% porosity (see discussion in Wieczorek and Phillips, 1997) we will employ an average value of 3100 kg m^{-3}.

We next choose the core radius, core density, and mantle density such that they are consistent with the lunar mass and moment of inertia (e.g., Hikida and Mizutani, 2005). For the core density, we assume a reasonable value of 6600 kg m^{-3}, which is representative of liquid iron with a small amount of light alloying elements. By utilizing a simple three-layer constant-density model of the Moon, and by treating the crust and core density as known, the mass and moment of inertia define a nonunique relationship for the acceptable values of the average crustal thickness, mantle density, and core radius. By choosing one value, the other two are uniquely determined. Here, we will choose the desired average crustal thickness and then compute the implied core radius and mantle density. We note that our chosen value for the core density has little influence on the average mantle density, and hence only minimally affects our crustal thickness model which depends principally on the density contrast at the crust–mantle interface.

We choose the average crustal thickness such that the minimum value of our inversion (excluding the mare basalt fill) is less than 1 km (a similar assumption for Mars was used by Neumann et al., 2004). While we could have chosen a larger (but not smaller) value, this approach is consistent with the expectation that at least one of the giant impact basins excavated into the mantle. This procedure gives rise to an average crustal thickness of about 43 km, a mantle density of 3360 kg m^{-3} and a core radius of 370 km. This average crustal thick-

ness is consistent with the range of 49 ± 16 km advocated by Wieczorek et al. (2006) that is based upon a variety of gravity, topography, and seismic considerations. Furthermore, while our utilized core density and radius are certainly not unique, we note that our adopted values are generally consistent with a number of recent geophysical and geochemical investigations (e.g., Konopliv et al., 1998; Hood et al., 1999; Williams et al., 2001; Kuskov et al., 2002; Righter, 2002; Khan et al., 2004, 2006; Khan and Mosegaard, 2005; Lognonné and Johnson, 2007).

Concerning the average crustal thickness, we note that we could have chosen this value such that our inversion results matched those obtained from analyses of the Apollo seismic data. While the original analysis suggested a crustal thickness of about 60 km in the vicinity of the Apollo 12 and 14 stations (Toksöz et al., 1974), recent analyses point to thinner values for the region of the Apollo seismic network of 45 ± 5 km (Khan et al., 2000), 38 ± 3 km (Khan and Mosegaard, 2002), and 30 ± 2.5 (Lognonné et al., 2003). Given the large spread of these estimates, we have not attempted to fit any specific model.

We next describe how we defined the coordinates used in the polyhedral shape models of the surface and crust–mantle interface. For each, we started with a regular icosahedron of 20 equilateral triangular patches. Each triangular patch was then recursively subdivided into 4 subtriangles until a desired spatial sampling was achieved (see Appendix A for further details). For the surface model, we divided each of the original 20 triangular faces into 4^5 faces, giving rise to a total of 20,480 faces and 10,242 vertices. The angular distance of each edge in this model is about 2 degrees, which corresponds to about 60 km on the lunar surface and a spherical-harmonic resolution close to degree 100. This corresponds approximately to the inherent spatial resolution of the employed Clementine shape model of the Moon. Each vertex was then assigned an absolute radius based on the 359-degree spherical-harmonic model USGS359 (USGS, 2002; Wieczorek, 2007). This model is based upon a combination of Clementine altimetry data and stereo photogrammetry over the lunar poles and possesses a significantly higher spectral correlation with the observed gravity field than the previous spherical-harmonic model GLTM2C (Smith et al., 1997).

For our shape model of the crust–mantle interface, we initial started by subdividing each of the 20 faces of a regular icosahedron into 144 triangular patches, leading to a total of 2880 triangular patches and 1442 vertices. The average distance between vertices is about 180 km, corresponding to a spherical-harmonic resolution of about 37. We note that the previous models of Wieczorek and Phillips (1998) and Wieczorek et al. (2006) filtered the Bouguer anomaly using a filter with a value of 0.5 at degree 30, demonstrating that our model has a higher spatial resolution. Experience has shown that this initial grid for the crust–mantle interface was not sufficient to fit everywhere the gravity field on the nearside of the Moon. In order to rectify this, we have increased the spatial resolution in the vicinity of the major impact basins and in regions where the crustal thickness changes rapidly. Furthermore, the resolution was increased over some regions on the nearside that originally gave rise to large differences between the observed and mod-
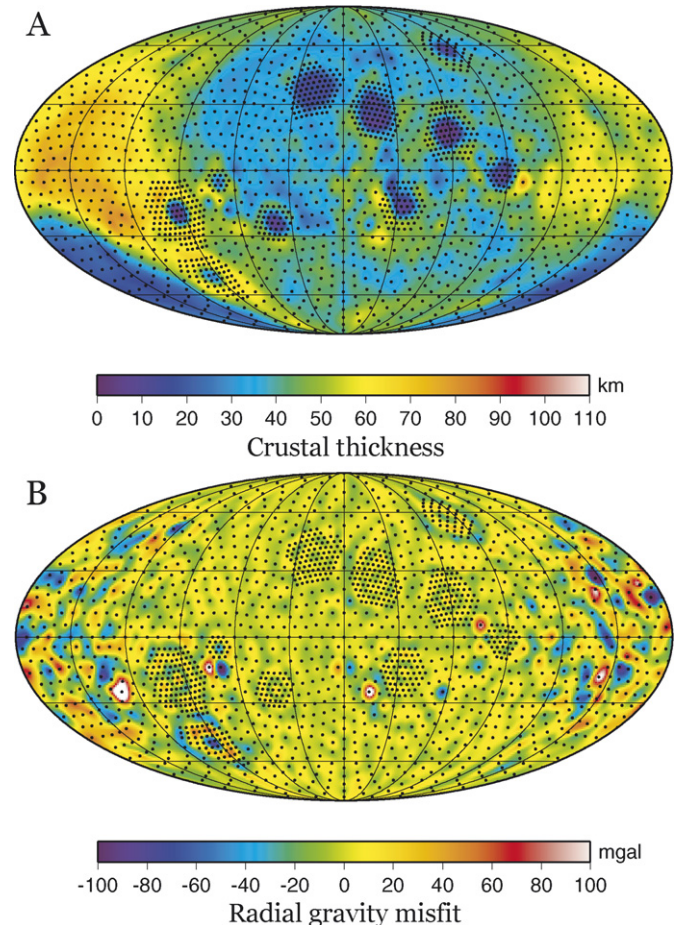

Fig. 2. Crustal thickness of the Moon derived from a polyhedral shape model inversion. (A) Crustal thickness excluding mare fill. The location of each vertex of the polyhedral model of the crust–mantle interface is shown as solid dots. (B) The difference between the observed and modeled radial gravity. Images are shown in a Mollweide projection with a central meridian of 0° longitude.

eled radial gravity. We use the latitude and longitude points of this model when calculating the misfit function of Eq. (9).

In generating our final crustal thickness model, we used the parameter values given in Table 1 and the mare basalt thickness model that was employed by Wieczorek and Phillips (1998), which is the mare basalt disk model of Solomon and Head (1980) revised by the maximum thickness estimates of Williams and Zuber (1998). Furthermore, we used the lunar shape model USGS359, the lunar gravity model LP150Q (Konopliv et al., 2001), and the gridded radial gravity uncertainties from the model JGM100J1. The spherical-harmonic representations of the gravity and topography were truncated beyond degree 90, as this corresponds approximately to the average resolution of the topography model.

Our final model is shown in Fig. 2A, where, for plotting purposes, we have used the GMT command `surface` (with $T = 0.25$; Smith and Wessel, 1990) to interpolate between vertices. Also shown are the locations of the vertices used in our crust–mantle shape model. In Fig. 2B, we plot the difference between the observed and modeled radial gravity. The average misfit for the nearside is seen to be about 15 mGals, whereas for the farside it is somewhat larger, about 30 mGals, with some re-

gions possessing differences up to 240 mGals. We note that the estimated errors in the radial component of the employed gravitational field are about 30 mGals for the nearside, and can reach up to 200 mGals for the farside (Konopliv et al., 2001). We estimate the uncertainties associated with our crustal thickness model utilizing the first-order Cartesian Bouguer slab formula (e.g., Turcotte and Schubert, 1982)

$$\Delta g = 2\pi G(\rho_{mantle} - \rho_{crust})\Delta h, \tag{12}$$

where Δh is the magnitude of relief at the crustal–mantle interface with a density contrast of $(\rho_{mantle} - \rho_{crust})$. Using our average nearside and farside data misfits of 15 and 30 mGal, we find that this corresponds to an uncertainty of about 0.5 and 1 km of mantle relief, respectively.

For comparative purposes, we have also calculated a crustal thickness model using the filtered spherical-harmonic inversion methodology of Wieczorek and Phillips (1998) with the same parameters as adopted for our polyhedral model. We have applied the same filter to the Bouguer anomaly as used in that paper, and plot this model in Fig. 3A. While the models are generally similar, as shown in Fig. 3B, the fit to the observed radial gravity is poorer than ours. Histograms of the difference in crustal thickness between these two models is shown in Fig. 4 over both the lunar near- and far-side hemispheres. The model differences over the nearside are most certainly a result of the filtering operation that was used to stabilize the spherical-harmonic inversion. While the standard deviation between the two models over this hemisphere is only about 3 km, important differences are evident where the crustal thickness changes rapidly, and can be as high as almost 20 km in some regions. In contrast, the larger differences that are found over the farside hemisphere are primarily a result of our model being smoother there, which is a direct consequence of having taken into account the uncertainties in the gravity field. The large oscillations evident in the filtered spherical-harmonic inversion are most likely a result of the amplification of measurement noise.

Finally, we address some of the model dependencies associated with our chosen set of input parameters. First, concerning the fidelity of the topography model, we have also performed a crustal thickness inversion using the GLTM2C spherical-harmonic model. While the USGS359 model is preferred (see Wieczorek, 2007), in part because it includes data over the poles obtained by stereo imaging, the difference in crustal thickness between the two is on average only 1.5 km. Nevertheless, in some regions, particularly over the poles, the difference can be more substantive, up to 12 km. Other regions with large differences correspond to gaps in the Clementine altimetry data and are related to different interpolation schemes used in constructing the USGS359 and GLTM2C models. Tests using the entirely photogrammetric topographic model ULCN2005 (Archinal et al., 2006), which possesses a higher spatial resolution and more even data coverage, yields results that are nearly identical to those based on USGS359.

Another source of error is related to our adopted mare basalt thickness model, and we evaluate this using the Cartesian Bouguer slab formula. With this approximation, we equate
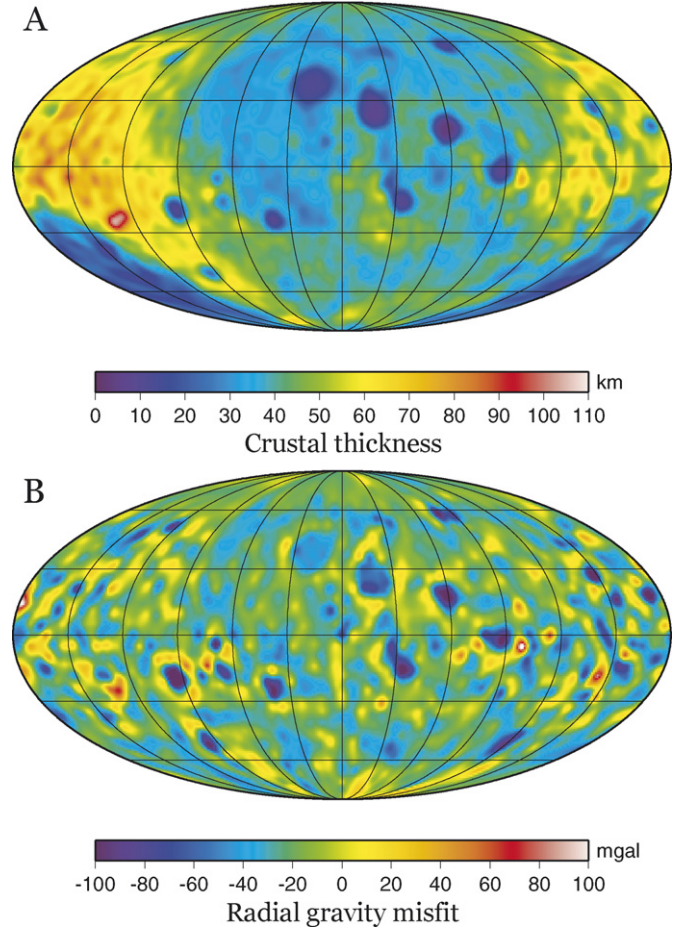

Fig. 3. Crustal thickness of the Moon derived from a filtered spherical-harmonic inversion using the same parameters as in Fig. 2. (A) Crustal thickness excluding mare fill. (B) The difference between the observed and modeled radial gravity.

the gravitational attraction of mare basalts with thickness h_{mare} and density contrast $(\rho_{mare} - \rho_{crust})$ to that of crust–mantle relief Δh of density contrast $(\rho_{mantle} - \rho_{crust})$, which yields the relationship

$$\Delta h = \frac{\rho_{mare} - \rho_{crust}}{\rho_{mantle} - \rho_{crust}} h_{mare}. \tag{13}$$

Using densities of 2800, 3100 and 3360 kg m^{-3} for the crust, mare basalts, and mantle, respectively, each kilometer of mare basalts is seen to correspond to a change of about 0.5 km of mantle relief. In the extreme situation where we were to have over- or under-estimated the mare basalt thickness by 6 km, the total crustal thickness would only change by about 3 km. Furthermore, the total crustal thickness excluding the mare basalts would also only change by about 3 km. Thus, for most purposes, any errors introduced into our crustal thickness model by the use of an inappropriate mare thickness model are relatively unimportant.

Finally, we note that Wieczorek and Phillips (1998, 1999) utilized a model of crustal structure that was stratified into upper anorthositic and lower noritic layers. Such a model was based on the possible existence of an intracrustal seismic discontinuity about 20 km below the surface (e.g., Toksöz et al.,
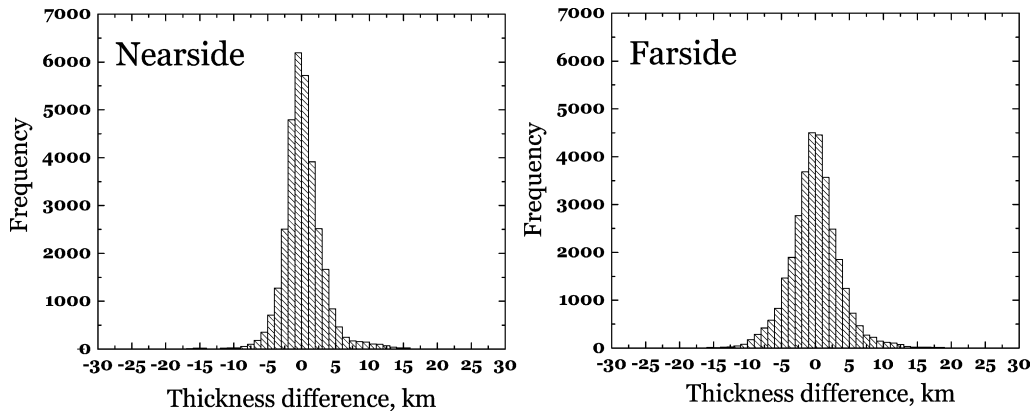
Fig. 4. Histograms of the difference in crustal thickness between the polyhedral and filtered spherical-harmonic inversions. The standard deviation over the near- and far-side hemispheres is 3 and 4 km, respectively.

1974), the mafic composition of some central peaks that are derived deep below the surface (Tompkins and Pieters, 1999; Wieczorek and Zuber, 2001), the mafic character of the floor of the South Pole–Aitken basin (Pieters et al., 1997), the common interpretation that the mafic impact melts were derived from the lower crust, and the relationship between the lunar geoid and topography over the lunar highlands (Wieczorek and Phillips, 1997). While more complicated crustal thickness models that take into account vertical variations in density might differ somewhat from the model presented here, Wieczorek and Phillips (1998) noted that the difference in total crustal thickness between their single and dual-layered models was not too great (the standard deviation between the two is only about 4 km).

4. Discussion

4.1. Global structure

Our crustal thickness model shares the same general attributes that have been noted by previous investigators (Zuber et al., 1994; Neumann et al., 1996; Wieczorek and Phillips, 1998; Potts and von Frese, 2003a; Wieczorek et al., 2006). In particular, the crust is seen to be substantially thinned beneath many of the large impact basins, and some of these are surrounded by rings of thickened crust. The structure of the giant impact basins will be discussed in greater detail in Section 4.3.

As a result of our assumption of a constant density crust, the higher elevations associated with the lunar farside hemisphere give rise to a thicker crust there. The axis of the thickened crust points towards (7° N, 156° W), and the average hemispheric crustal thickness difference with respect to this axis is 7.4 km. The direction of this hemispheric variation coincides approximately with the Earth–Moon axis, and hence can be described approximately as a nearside–farside crustal thickness dichotomy. Nevertheless, as discussed in Wieczorek et al. (2006), if lateral variations in crustal and mantle density exist between the near- and far-side hemispheres, these might act to reduce the magnitude of such an effect. Several lines of evidence exist suggesting that the two hemispheres are somewhat compositionally distinct (see Jolliff et al., 2000), but lacking in-

dependent estimates as to the magnitude of lateral variations in density, we cannot easily account for this in our models.

Our crustal thickness model is considerably smoother over the farside hemisphere than previous spherical-harmonic based models. This, however, is most likely a consequence of our having taken into account the larger gravitational uncertainties there, and is not necessarily real. Direct gravitational constraints over the farside, as will be obtained from the upcoming Japanese mission SELENE (Kato et al., 2007), will be necessary to investigate shorter wavelength features that might be present there. In contrast to the farside hemisphere, relative variations in crustal thickness are somewhat larger for our model over the nearside than previous models, particularly beneath the giant impact basin (see Section 4.3 and Fig. 6). This is simply a result of short wavelength features having been damped by the filtering procedure used in previous spherical-harmonic based models.

The minimum crustal thicknesses in our model, after excluding the mare basalt fill, are found within the Orientale and Crisium basins with values of 0.7 and 0.8 km, respectively. Previous models based on filtered spherical-harmonic inversions obtained minimum crustal thicknesses close to zero only beneath the Crisium basin. Though our model was constructed by requiring the minimum thickness to be close to zero, these two basins, nevertheless, should be considered as good candidates for having potentially excavated all the way through the crust and into the mantle. Given our uncertain knowledge of lateral variations in crustal and mantle density, the average thickness of the crust, the thicknesses of the mare basalts, and uncertainties in the gravity model, it is probably reasonable to expect that our crustal thickness model possesses absolute uncertainties on the order of 5 km. Using this number as a guide, not only could have the Orientale and Crisium basins excavated into the mantle, but so could have Humorum and Humboldtianum.

4.2. Comparison with seismic constraints

Our crustal thickness model was constructed based on assumptions about the crustal and mantle density, combined with the constraint that the minimum crustal thickness (excluding mare basalt fill) is close to zero. As no seismic information
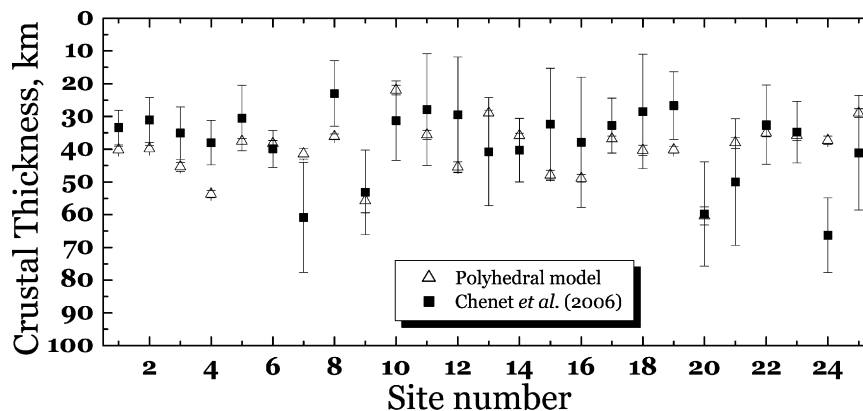
Fig. 5. Comparison of the crustal thicknesses obtained from a polyhedral shape model inversion and the seismic results of Chenet et al. (2006). The first four sites correspond to the Apollo stations 12, 14, 15 and 16, and the rest are for meteoroid impacts.

was input into our model, we here quantify how well our model compares to the available seismic constraints. Such constraints include estimates of the crustal thickness in the vicinity of the Apollo 12 and 14 stations, the region of the Apollo seismic network, and at a variety of meteoroid impact sites.

We first note that the original analysis of the Apollo seismic data suggested a crustal thickness of about 60 km (Toksöz et al., 1974) for the Apollo 12 and 14 landing sites, which lie within about 155 km of each other. Our model, in contrast, predicts a thinner average crustal thickness at these two sites of about 40 km. Recent analyses of the seismic data suggest that the crustal thickness in the region of the Apollo seismic network is probably considerably thinner than once though. Khan et al. (2000) and Khan and Mosegaard (2002) first proposed values of 45 ± 5 km and then 38 ± 3 km that should be taken as being representative of the area surrounding the Apollo seismic network, which includes Apollo 12, 14, 15, and 16. In a similar analysis, Lognonné et al. (2003) obtained a value of 30 ± 2.5 km, though it should be noted that this estimate places somewhat more emphasis on the structure beneath the Apollo 12 station. An analysis by Chenet et al. (2006) obtained an average of 34 ± 7 km for the four Apollo stations using the seismic velocity model of Gagnepain-Beyneix et al. (2006) combined with the artificial and natural impact events (see below). Our inversion predicts an average value of about 44 km beneath the four Apollo seismic stations, which is generally compatible with, though somewhat higher than, these recent analyses.

In addition to the seismic studies mentioned above, one investigation has attempted to place constraints on the crustal thickness at the Apollo 16 site. Goins et al. (1981) performed an analysis of putative converted phases at this site and obtained a crustal thickness of 75 km. In contrast, our model predicts a crustal thickness of 54 km. The recognition of converted phases at this site is somewhat contentious (Chenet et al., 2006), and the reported crustal thickness estimate is clearly inconsistent with our model.

The only study that has attempted to place constraints on the crustal thickness far from the Apollo seismic network is that of Chenet et al. (2006). In their study, seismic signals induced by artificial and natural meteoroid impacts were used to constrain the crustal thickness beneath both the impact sites and Apollo

stations. In order to make their inversion tractable, it was necessary to assume that the seismic velocity of the crust and upper mantle was everywhere the same, for which they used the average velocities from the model of Gagnepain-Beyneix et al. (2006). The differences between observed and predicted first arrival times were then modeled by variations in crustal thickness. Crustal thickness estimates were obtained at 25 locations, including 2 artificial impact sites, 19 meteoroid impacts, and the 4 Apollo stations. These sites are generally located on the nearside of the Moon, though a few of the most distant impacts are located beyond the lunar limbs.

In Fig. 5, we compare the crustal thicknesses obtained from our polyhedral model to the seismic results of Chenet et al. (2006). The site numbers correspond to those in Tables 2 and 3 of that paper, and here we only note that the first 4 sites correspond to the Apollo 12, 14, 15 and 16 stations, respectively. The two models are broadly consistent, with 17 of the 25 sites being within one standard deviation of each other. In particular, we note that the reduced chi-squared misfit of the two distributions is equal to 1.18, whereas the expected value should be 1 ± 0.29 (e.g., Press et al., 1992). Nevertheless, a few locations compare poorly. In particular, we predict somewhat higher crustal thicknesses for the Apollo landing sites, and the Apollo 16 station and impact site 24 are somewhat discordant. It is important to note that the crustal thickness estimates of Chenet et al. (2006) are dependent on the crustal and mantle velocities that were employed in their inversion and that different values might perhaps give a better fit.

4.3. Impact basin structure

As is clearly visible in Fig. 2, the most dramatic crustal thickness variations on the Moon are associated with large impact basins. In this section we characterize the structure of both young and old impact basins, and estimate the size of their excavation cavities—that portion of the crust that was ballistically excavated during the cratering process. Our methodology parallels closely that of Wieczorek and Phillips (1999) in that the geometry of the excavation cavity will be approximated to first order by restoring the uplifted crust–mantle interface beneath these basins to its (assumed horizontal) pre-impact position; the
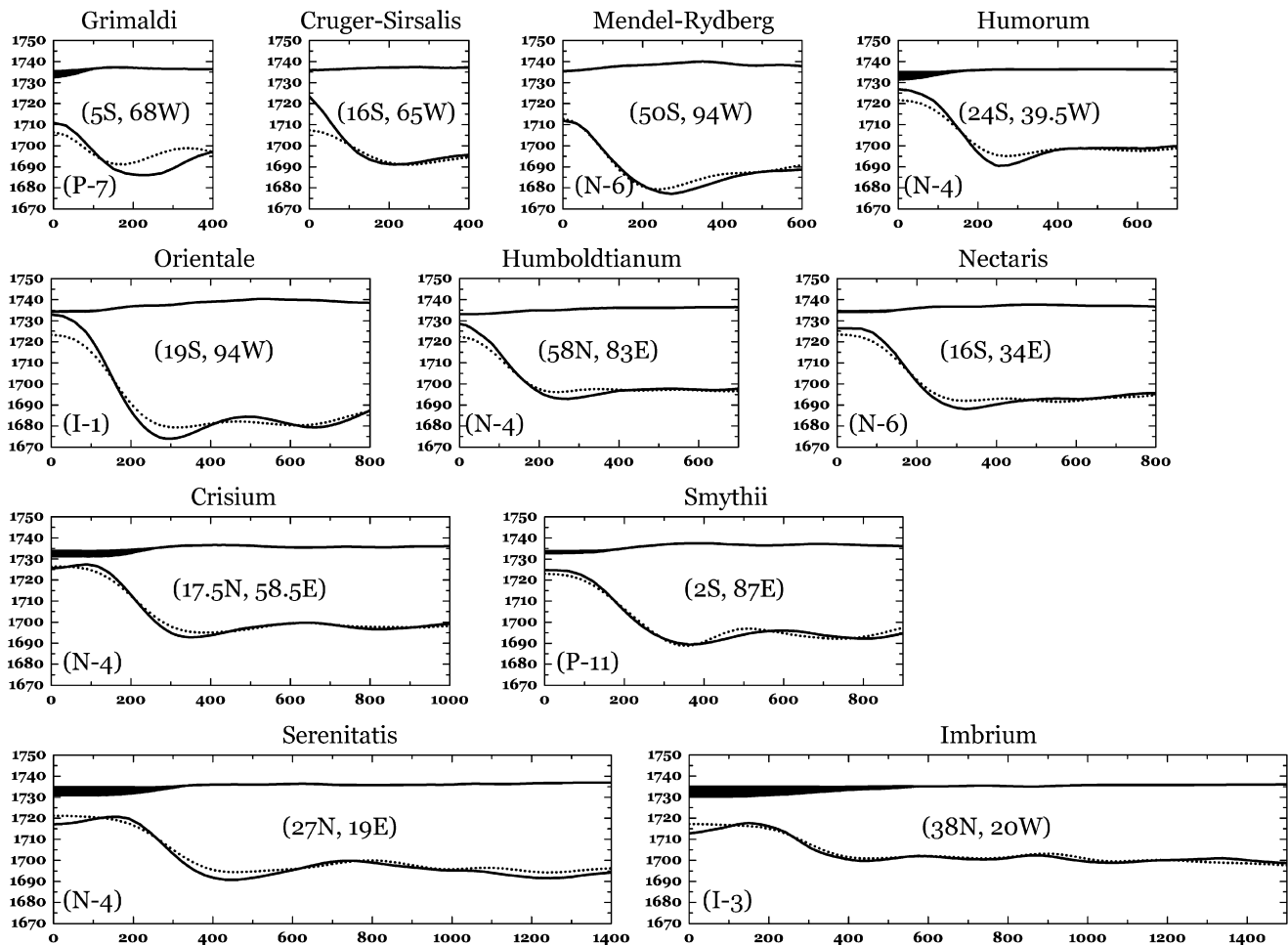
Fig. 6. Azimuthally averaged crustal thickness profiles of the major young impact basins. Vertical axes are radial distance from the center of the Moon, and horizontal axes are the radial distance from the center of each basin. Black colored regions represent mare fill, the upper solid line is the surface topography, the subsurface solid line is the crust–mantle interface from the polyhedral inversion, and the dashed line is the crust–mantle interface obtained from the filtered spherical-harmonic inversion. Age classification using the notation of Halekas et al. (2003) and the center of the basin are indicated. All plots possess the same scale.

reader is referred to that paper for a more detailed discussion. Knowledge of the size of the excavation cavity can be used to estimate various quantities such as the depth of excavation, the transient cavity radius, and the mass and volume of excavated materials.

We will first discuss those basins with good gravity coverage that are as young or younger than Smythii [i.e., age group 5 of Wilhelms (1987), see also Wilhelms (1984)] and which have diameters larger than 365 km (the approximate resolution of the crustal thickness model). Of these basins, two are Imbrian in age (Imbrium and Orientale), six are Nectarian (Serenitatis, Crisium, Humorum, Humboldtianum, Mendel–Rydberg, and Nectaris), and two are pre-Nectarian (Grimaldi and Smythii). The Cruger–Sirsalis basin (Cook et al., 2002) will additionally be considered because of its remarkable crustal thinning. Although the relative age of this basin is not well known, it appears to be younger than the Grimaldi basin, but older than the Orientale basin (Paul Spudis, personal communication). The centers for most basins were taken from the geologic mapping of Wilhelms (1987), with the exceptions of Orientale, Imbrium, Humboldtianum and Cruger–Sirsalis that were estimated from our crustal thickness model.

Radially averaged basin profiles are shown in Fig. 6 for these basins using both our polyhedral (solid lines) and spherical-harmonic based (dashed lines) crustal thickness models. These are plotted in reverse order of their reconstructed excavation cavity diameter, as determined below, and the age classification following the numbering scheme of Halekas et al. (2003) is indicated (groups of impact basins increase in age from 1 to 15, and the number is preceded by I, N, or P, signifying Imbrian, Nectarian, or pre-Nectarian, respectively). While the two crustal thickness models are generally similar, the amount of predicted uplift of the crust–mantle interface beneath the Humorum, Orientale, Humboldtianum and Cruger–Sirsalis basins is clearly larger for our polyhedral model.

As discussed in Wieczorek and Phillips (1999), we will assume that the crust mantle interface rebounded in a purely vertical fashion following the excavation stage of the cratering process. We assume that the crust–mantle interface was originally flat, here approximated by the average depth at three excavation cavity radii, and simply "restore" this interface to its original presumed horizontal pre-impact position by a vertical translation. The resulting cavity, which is generally parabolic,

Table 2
Reconstructed excavation cavity measurements for the young nearside impact basins

| Basin	Age	Polyhedral model		Filtered spherical harmonic inversion	
		Diameter (km)	Depth (km)	Diameter (km)	Depth (km)
Grimaldi	P-7	206 ± 4	18.1 ± 1.7	204 ± 6	14.7 ± 1.8
Cruger–Sirsalis	–	306 ± 20	27.8 ± 5.1	392 ± 20	15.8 ± 2.2
Mendel–Rydberg	N-6	337 ± 13	29.4 ± 2.9	302 ± 10	28.4 ± 2.9
Humorum	N-4	382 ± 6	33.4 ± 1.3	431 ± 15	29.0 ± 1.7
Orientale	I-1	383 ± 5	46.9 ± 1.6	418 ± 8	38.4 ± 1.4
Humboldtianum	N-4	394 ± 18	33.0 ± 3.6	486 ± 34	26.8 ± 4.2
Nectaris	N-6	455 ± 5	34.9 ± 1.9	468 ± 10	30.3 ± 1.3
Crisium	N-4	560 ± 2	34.6 ± 3.7	611 ± 15	35.3 ± 2.2
Smythii	P-11	567 ± 19	36.5 ± 1.5	580 ± 14	35.4 ± 1.3
Serenitatis	N-4	718 ± 22	28.8 ± 3.9	745 ± 5	30.5 ± 2.4
Imbrium	I-3	895 ± 11	21.1 ± 3.7	901 ± 5	23.5 ± 1.8

Fig. 7. Reconstructed excavation cavity depth as a function of its diameter. Best fit line excluding the two largest basins (Imbrium and Serenitatis) is $h_{ex} = (0.083 \pm 0.002)D_{ex}$. The shaded area is the range of ambient crustal thicknesses for these basins at three excavation cavity radii.

is assumed to approximate the first order geometry of the basin excavation cavity.

In order to estimate the depth and diameter of the excavation cavity, we employ two methods. First, we simply fit the shape of the depression using a parabolic function, from which the depth and diameter are easily obtained. Since some basins are poorly approximated by a parabolic form, we also estimate the depth and diameter using the depth at the basin center and the diameter at which the excavation cavity is first equal to the surrounding average surface elevation. Here, we quote the average from these two methods and the "uncertainty," which is half of their difference, in Table 2. Finally, concerning the depth estimates, we added in quadrature the uncertainty in crustal thickness that is expected from the uncertainty in the gravity field [see Eq. (12)].

We note that this method of reconstructing the excavation cavity ignores several processes and complications, but that these are likely to have magnitudes that are comparable to the uncertainties associated with our crustal thickness model. In particular, gravitational collapse of the crater wall would tend to increase its diameter, and this methodology would thus overestimate the excavation cavity diameter. Nevertheless, it has been noted that the relative importance of wall collapse appears to decrease with increasing crater diameter (Pike, 1976). If some of the basin ejecta were to fall back into the crater, this method would slightly underestimate the excavation depth. The biggest uncertainty with this methodology concerns the fact that the excavation flow field set up during the excavation stage will displace some crustal materials radially away from their original position (Melosh, 1989; O'Keefe and Ahrens, 1993). We can not easily quantify this effect, but suspect that this will not dramatically affect our results. The effects of viscous relaxation and having excavated through the entire crust will be discussed later. Finally, we note that the presence of an impact melted crust and/or mantle below the excavation cavity will not affect our geometric reconstructions as long as this material does not flow laterally from its pre-impact position. Even if our reconstructed depths and diameters were to be systematically biased by a small factor, to first order, this should affect all craters equally.
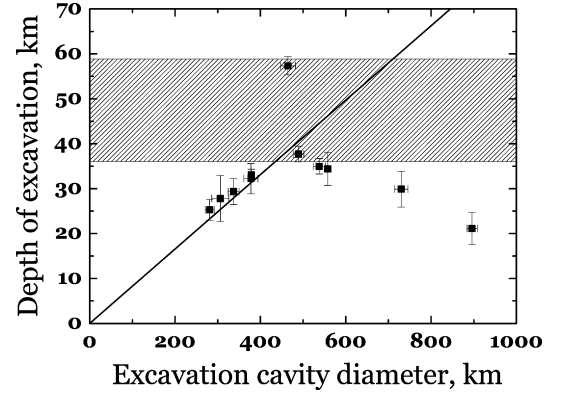
Fig. 7 plots the depth–diameter relationship of the reconstructed excavation cavity for the 11 basins shown in Fig. 6. For reference, the ambient crustal thickness surrounding these basins at three excavation cavity radii is shown by the shaded region in this plot. With the exception of the two largest basins (Imbrium and Serenitatis), the depth of excavation generally increases with increasing excavation cavity diameter. Excluding Imbrium and Serenitatis, the best fit straight line (constrained to pass through the origin) is found to be $h_{ex} = (0.083 \pm 0.002)D_{ex}$, where h_{ex} and D_{ex} are the depth and diameter of the excavation cavity, respectively. This result is generally consistent with craters ranging in size from centimeters to several tens of kilometers in diameter which all yield depth/diameter ratios of the excavation cavity close to 0.1 (Croft, 1980; O'Keefe and Ahrens, 1993). We note that Wieczorek and Phillips (1999) originally obtained a depth/diameter ratio of 0.115 ± 0.005 using this same methodology, which is slightly larger than our estimate. This is related primarily to their having used the Apollo-era seismic constraint of 60 km at the Apollo 12 and 14 sites in constructing their crustal thickness model, which is now recognized to be too large.

We briefly comment on the apparently anomalous excavation cavities of the Imbrium and Serenitatis basins. As discussed by Wieczorek and Phillips (1999, 2000), these basins appear to have impacted into an anomalous geochemical province rich in incompatible elements, a region now referred to as the Procellarum KREEP Terrane (see also Jolliff et al., 2000; Korotev, 2000). The Imbrium basin clearly resides within the confines of this province, whereas the Serenitatis basin borders this and the adjacent Feldspathic Highlands Terrane. Thermal evolution models based on reasonable geochemical constraints (Wieczorek and Phillips, 2000) suggest that the heat flow within the Procellarum KREEP Terrane could have been several times larger than that of the surrounding regions. Thus, it is plausible that high temperatures could have led to enhanced rates of viscous relaxation, leading to the slow lateral transport of crustal materials into the basin center. Nevertheless, as shown by Mohit and Phillips (2006), viscous relaxation, even in the presence of a hot crust, is difficult to achieve for regions where the crust is thin.
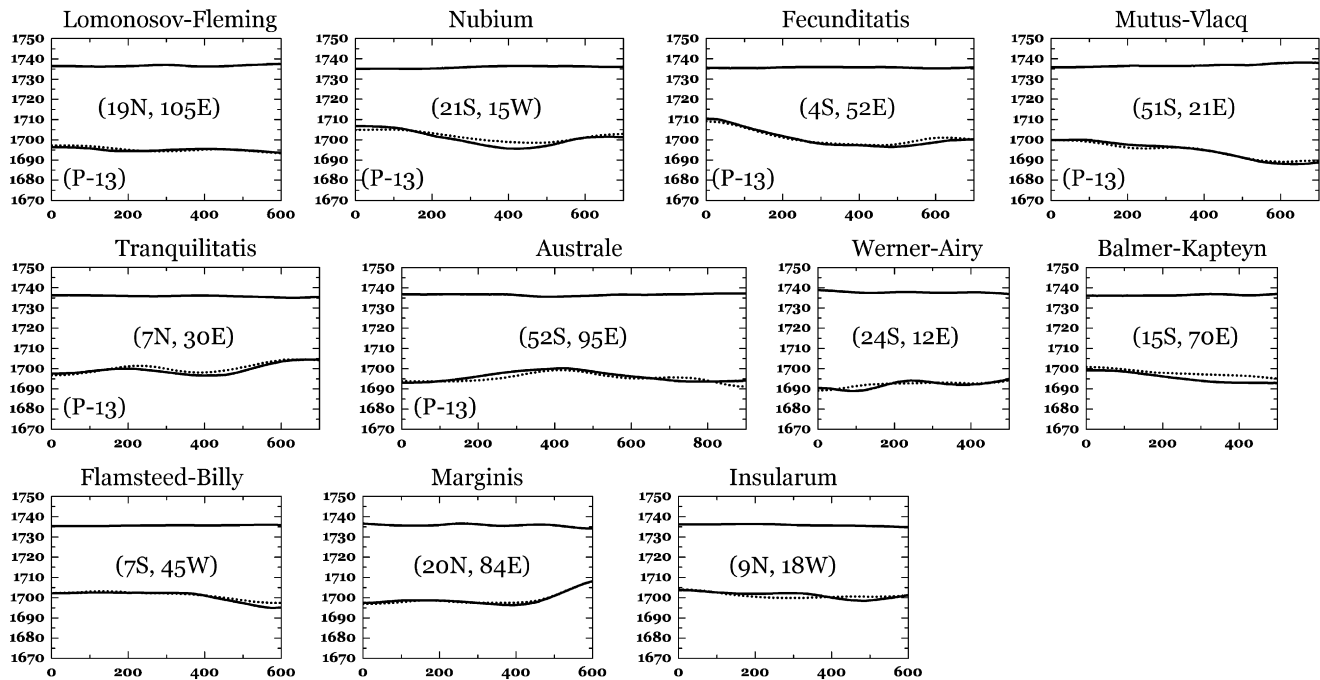
Fig. 8. Azimuthally averaged crustal thickness profiles for the major pre-Nectarian impact basins. Basin centers taken from Wilhelms (1987).

Alternatively, as discussed by the same authors, it is possible that the lunar magma ocean had not completely crystallized beneath the Procellarum KREEP terrane at the time of these impacts (3.89 ± 0.01 Ga for Serenitatis, Dalrymple and Ryder, 1996; 3.85 ± 0.02 Ga for Imbrium, Ryder, 1994). It has long been recognized that the last remaining dregs of the magma ocean could have remained molten for about a billion years as a result of its high concentration of incompatible elements (e.g., Solomon and Longhi, 1977; Wieczorek and Phillips, 2000). If the Imbrium and Serenitatis basins excavated all the way through the crust, this magma, if present at these locales, could have flown into the excavation cavities of these two basins. If the solidified magma had a density similar to that of the crust, such a phenomenon would artificially reduce the reconstructed excavation depths of these basins using our methodology.

The crustal structure of basins that are older than those considered above, and which should be resolved in our crustal thickness model, are shown in Fig. 8. While the absolute ages of these basins are unknown, stratigraphically they are older than the Nectaris basin, which is believed by many to have formed at 3.93 Ga (e.g., Spudis, 1993), though an age as old as 4.1 Ga is possible (e.g., Haskin et al., 1998; Korotev et al., 2002). As is seen, the crust–mantle interface beneath these basins is relatively flat, and if any crustal thinning is present, this is generally restricted to variations of less than 10 km. Since there is no reason why these impact basins would not also have excavated deeply into the crust, their lack of any significant crustal thinning is most likely attributable to post-impact modification processes.

Given the old pre-Nectarian ages of these basins, it is likely that the crust was hotter when they formed than it was for the basins younger than Smythii. Indeed, for the oldest of these basins, it is possible that the magma ocean had not yet even fully crystallized. Higher temperatures at this time could have plausibly given rise to the viscous relaxation of any crustal thickness variations that might originally have been present (see Mohit and Phillips, 2006). From a geophysical standpoint, it thus appears that the rheologic behavior of the crust was significantly different before the Smythii impact event than afterwards. This is almost certainly related to the thermal regime that these basins were subjected to shortly after the formation of the crust, and if the absolute ages of these basins could be determined, this fact could be used to place constraints on the early thermal evolution of the Moon.

Finally, it is noted that the crust–mantle interface beneath the Nectaris, Crisium, and Smythii basins appears to be horizontal in the central portion of these craters. Furthermore, the crustal thickness is predicted to be fairly thin at these locations, less than about 10 km. Such a structure could arise if these basins excavated all the way through the crust and into the mantle, and if for some reason we were systematically overestimating the crustal thickness in these regions. By choosing different values for the crustal and mantle densities, at least locally, it is probable that crustal thickness inversions could be obtained where the crust was nearly absent beneath these craters. If these craters did excavated though the entire crust, then our reconstructed excavation cavity depths should be considered as minimum values.

4.4. Isostatic state of lunar impact basins

Large positive gravity anomalies on the Moon, referred to as "mascons," were discovered at the centers of many basins during the Apollo era (Muller and Sjogren, 1968). A common explanation for this observation is that (1) the impact basins were initially in a state of isostatic equilibrium, and (2) when the mare basaltic lava flows erupted hundreds of millions of

years later, the lithosphere was thick enough to support the stresses associated with these loads over geologic time (e.g., Solomon and Head, 1980; Bratt et al., 1985).

While the mare basalts certainly contribute to the observed gravitational signature of these basins, it has been suggested that the mascons might instead have their origin primarily in the uplift of the crust–mantle interface beneath these basins (Neumann et al., 1996; Wieczorek and Phillips, 1999). This hypothesis requires the mantle uplift to be superisostatic (i.e., uplifted beyond its natural isostatic position), and in support of this interpretation, Konopliv et al. (2001) have identified several mascon basins that do not appear to show evidence for mare volcanism. In this context, it should be noted that the largest expanse of mare volcanism, Oceanus Procellarum, shows no significant positive gravitational anomaly.

In this section, we quantify the isostatic state of the young nearside basins as is implied by our crustal thickness model. The net load acting on the lithosphere is calculated according to the equation (e.g., Belleguic et al., 2005)

$$q = g_0 \big[\rho_{\text{crust}} h_1 + (\rho_{\text{mantle}} - \rho_{\text{crust}}) h_2 + (\rho_{\text{mare}} - \rho_{\text{crust}}) h_{\text{mare}} \big], \quad (14)$$

where g_0 is the gravitational acceleration at the lunar surface, h_1 is the surface relief referenced to the geoid at the mean radius of the Moon, and h_2 is the amount of mantle uplift referenced to an equipotential surface at the mean radius of the crust–mantle interface. The first term accounts for the load due to surface topography, the second is the load resulting from relief along the crust–mantle interface, and the third is the load of the mare basalts. The shape of the equipotential surfaces at the mean surface radius and crust–mantle interface were estimated using first order theory, and the contribution resulting from the centrifugal and tidal potentials was explicitly taken into consideration.

Fig. 9A shows our estimated vertical load that is acting on the lunar lithosphere (positive stresses are directed downward). As is seen, large portions of the lunar crust are consistent with being isostatic (i.e., the net load is close to zero). In contrast many of the nearside impact basins are seen to be supporting large positive loads in their basin center, and some of these positive loads (most notably Orientale) are surrounded by negative loads. The negative annuli surrounding some basins are potentially interpreted as being a result of lithospheric flexure. In this scenario, the positive loads in the basin center have simply flexed the surrounding crust and lithosphere downward.

To determine whether the large lithospheric loads associated with the nearside impact basins are solely a result of mare basaltic lava flows superposed on a completely rigid lithosphere, we subtract the load associated with the basalts and plot this result in Fig. 9B. This naturally reduces the magnitude of the net load where basalts are present. In particular, the net load beneath Imbrium and Serenitatis is almost completely erased, suggesting that these basins were in a state of isostatic equilibrium before these lavas erupted. The slight negative load associated with the Imbrium basin is either due to our mare basalt thickness model being somewhat overestimated at this lo-
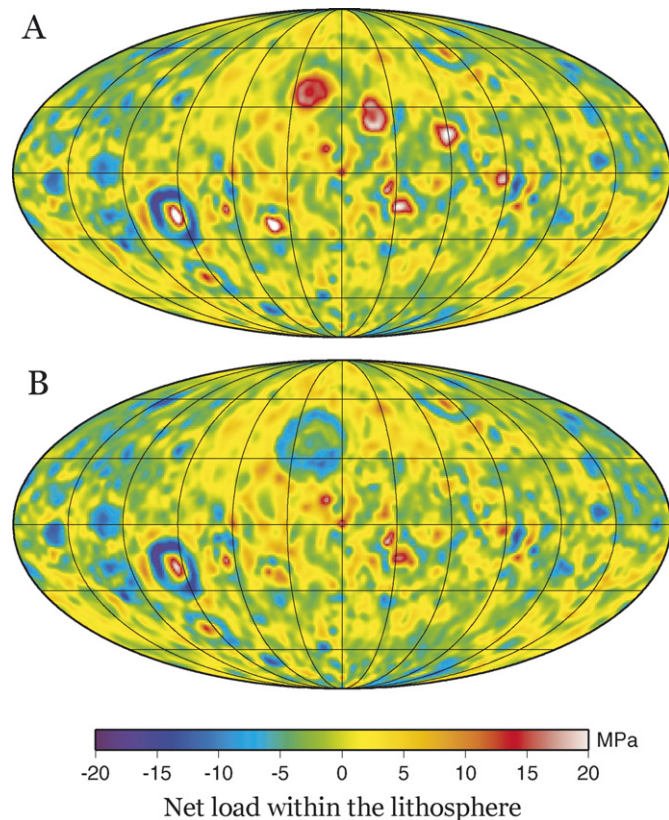

Fig. 9. The net load acting on the lithosphere (A) with and (B) without the contribution of the mare basalts.

cale, or that the load associated with these lavas gave rise to a small amount of lithospheric flexure.

Some basins such as Orientale, Nectaris, Smythii, and Humboldtianum, are still seen to be supporting a downward directed lithospheric load, even after the load of the mare basalts is removed. These excess loads are plausibly interpreted as resulting from superisostatic uplift of the mantle that could have occurred as the basin floor rebounded following the excavation stage of crater formation (see Neumann et al., 1996; Wieczorek and Phillips, 1999). Superisostatic uplift could conceivably be a consequence of the brief time period where acoustic fluidization operated following the impact event (Melosh, 1979). Alternatively, it is possible that this signature could be related to voluminous basaltic intrusions in the crust, or errors associated with our mare basalt thickness model. However, if this were the case, the required amount of additional mare basalts would correspond to a layer about 4 km in thickness. As the crust is very thin beneath these basins, this hypothesis would imply that a large portion (about half) of the crust should be composed of basaltic intrusions.

In Fig. 10, the maximum magnitude of the lithospheric load including (solid squares) and excluding (open squares) the mare basalts is plotted as a function of the basin excavation cavity diameter. This figure demonstrates that there is no apparent correlation between load magnitude and basin size. There is also no apparent correlation between load magnitude and basin age. One possible correlation is that the magnitude of the currently supported lithospheric load might be dependent on distance
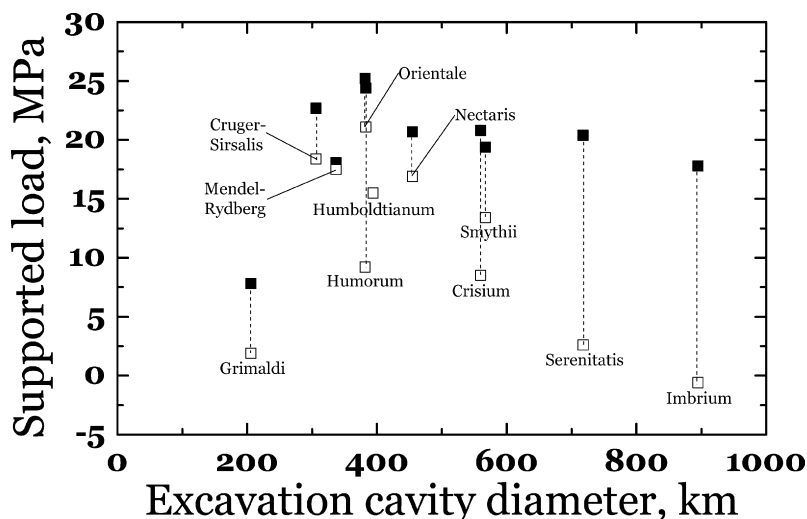
Fig. 10. The maximum magnitude of the lithospheric load including (solid squares) and excluding (open squares) the mare basalts as a function of the basin excavation cavity diameter.

from the Procellarum KREEP Terrane (Wieczorek and Phillips, 1999). In particular, the higher temperatures that are expected within the crust of this province might have helped relax deviatoric stresses there. Consistent with this suggestion, we note that most basins supporting loads less than 10 MPa are located within, or on the edge of, the Procellarum KREEP Terrane, and that larger stresses are supported beneath basins removed from this terrane. One exception to this rule is the Cruger–Sirsalis basin. Nevertheless, given its location next to Oceanus Procellarum, it is possible that this basin could possess mare basalts within its interior that were subsequently covered by ejecta from the adjacent Orientale basin, and which were not taken into account in this analysis. Radar observations appear to be consistent with this hypothesis (Campbell and Hawke, 2005).

5. Conclusions

As a result of the lack of spacecraft tracking data over much of the farside of the Moon, the lunar farside gravity field is much more poorly characterized than that of the nearside. In particular, while spherical-harmonic models of the gravity field have been developed up to degree 150, large portions of the farside possess spatial resolutions corresponding to about degree 15 (Konopliv et al., 2001). Given this highly variable spatial resolution, geophysical investigations that employ the use of global spherical-harmonic basis functions sometimes possess numerical instabilities that render global solutions unreliable. For the case of generating global crustal thickness models, this can be partially mitigated by applying a spectral filter to the Bouguer anomaly. However, as a result of the filtering operation, it is not possible to fit exactly the observed gravity field and the solution everywhere possess the same spatial resolution.

In this paper, we have developed a method of inverting for the crustal thickness of the Moon in the space domain using the formalism of Werner and Scheeres (1997) that allows for the exact calculation of the gravity field exterior to a uniform density polyhedron. Given this space domain approach, we are able

to tailor the spatial resolution of the crustal thickness model where necessary, and it is possible to weight the gravity measurements by their uncertainties in our inversion. While our resulting crustal thickness model is generally comparable to those of previous investigations, the spatial resolution of our model over the nearside basins is much higher, the misfit between the observed and modeled gravity are lower, and our solution is more faithful to the inherent variability in resolution of the gravity field.

Using our crustal thickness model, we have reinvestigated the crustal structure of the large nearside impact basins. Following the approach of Wieczorek and Phillips (1999), we have determined that the excavation cavities for most of the young impact basins possess a depth–diameter ratio of 0.083 ± 0.002. The crustal thickness (excluding mare basalts) is close to zero in the center of both the Orientale and Crisium basins, raising the possibility that these impact events could have excavated all the way through the crust and into the upper mantle. Given the uncertainties in our employed model parameters, the thin crust beneath the Humorum and Humboldtianum basins and the shallow horizontal crust–mantle interface beneath the Nectaris and Smythii basins is suggestive of these basins having excavated into the mantle as well. While the Imbrium and Serenitatis basins appear to posses anomalous crustal signatures, it is likely that these were affected by post-impact modification processes (i.e., viscous relaxation and/or magmatic infilling) related to their formation within the Procellarum KREEP Terrane, a province that is highly enriched in incompatible and heat producing elements. If the excavation cavity of Imbrium and Serenitatis possessed the same geometry as the smaller basins, these would have excavated significant quantities of mantle materials. Basins older than the Smythii basin possess little to no crustal structure, and this is likely to be a consequence of high crustal temperatures and higher rates of viscous relaxation that occurred early in the Moon's evolution.

The lithosphere surrounding many basins is found to be supporting net vertical loads on the order of 30 MPa, even after the

contribution of the mare basalts is removed. In general, those basins that lie closest to the Procellarum KREEP Terrane are those that are closest to approaching a pre-mare isostatic state. The excess loads that these basins are supporting, after removing the contribution of the mare basalts, is plausibly interpreted as superisostatic uplift of the mantle that was frozen into the lithosphere during rebound of the crater floor.

Finally, we note that our methodology of inverting for the crustal thickness of a planet is applicable to any body that possesses large variations in quality of the observed gravitational field. In particular, we note that both the gravitational field and topography of Mercury will be measured by the upcoming missions MESSENGER (Solomon et al., 2001) and BepiColumbo (Milani et al., 2001). However, for the first mission, MESSENGER, these will only be well characterized over the northern hemisphere of this planet.

Acknowledgments

Appendix A. Polyhedron construction

Following the methodology of Sadourny et al. (1968), we here describe how to determine the coordinates of a polyhedron composed of triangular faces. These coordinates will then be used to define the polyhedral models for the shape of the Moon and crust–mantle interface.

We begin with a regular icosahedron consisting of 20 equilateral triangular faces and 12 vertices, with vertices present at both poles. To increase the number of vertices, we subdivided each triangular face into four subtriangles (see Fig. 11). As an example, consider one triangular patch whose vertices are given by the vectors $\boldsymbol{Q}_1$, $\boldsymbol{Q}_2$, and $\boldsymbol{Q}_3$. If a vertex is placed at the midpoint of each edge of the triangle, then four triangles can be defined by $(\boldsymbol{Q}_1, \boldsymbol{Q}_4, \boldsymbol{Q}_6)$, $(\boldsymbol{Q}_2, \boldsymbol{Q}_5, \boldsymbol{Q}_4)$, $(\boldsymbol{Q}_3, \boldsymbol{Q}_6, \boldsymbol{Q}_5)$, and $(\boldsymbol{Q}_4, \boldsymbol{Q}_5, \boldsymbol{Q}_6)$, where

$$\boldsymbol{Q}_4 = \frac{\boldsymbol{Q}_1 + \boldsymbol{Q}_2}{2}, \qquad \boldsymbol{Q}_5 = \frac{\boldsymbol{Q}_2 + \boldsymbol{Q}_3}{2},$$

$$\boldsymbol{Q}_6 = \frac{\boldsymbol{Q}_3 + \boldsymbol{Q}_1}{2}. \tag{A.1}$$

Projecting the points $\boldsymbol{Q}_4$, $\boldsymbol{Q}_5$, and $\boldsymbol{Q}_6$ onto the unit sphere yields the vectors $\boldsymbol{Q}_4'$, $\boldsymbol{Q}_5'$, and $\boldsymbol{Q}_6'$, which define four triangular patches.

Following the above procedure, each new triangular face can be once more subdivided into four additional triangular faces. We note the resulting edges connecting the triangular faces are only quasi-equally spaced, as the subdivided triangles that are projected onto the unit sphere are no longer equilateral. Nevertheless, for our initial surface and crust–mantle interface grids, the edge lengths are nearly equally, with lengths of 66 ± 4 and 175 ± 11 km, respectively.
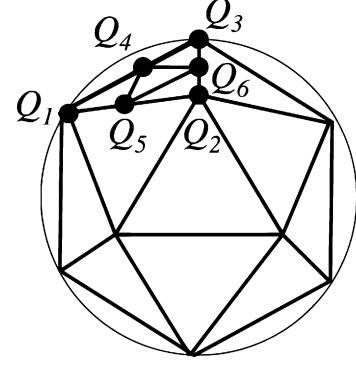

Fig. 11. Geometry of a polyhedral shape model based on subdividing the triangular patches of a regular icosahedron.

Appendix B. Calculation of the misfit gradient function

In order to use the Polak–Ribière conjugate gradient method, it is necessary to calculate the gradient of the misfit function. As shown by Eq. (11), this is dependent on the partial derivatives of the radial component of the gravitational field of a polyhedron with respect to the radii of its vertices, which we here give analytic expressions. As discussed in Section 2, the radial component of the gravitational field exterior to a constant density polyhedron can be calculated by performing two sums, one over all of the edges of the polyhedron, and the other over all of its faces. Therefore, the partial derivative of the radial gravity at observational position i with respect to the radius at coordinate j can be written as

$$\frac{\partial g_i}{\partial r_j} = \sum_{\text{edges}} \frac{\partial g_i^E}{\partial r_j} + \sum_{\text{faces}} \frac{\partial g_i^F}{\partial r_j}, \tag{B.1}$$

where g_i^E and g_i^F refer to the individual terms in the sums over the edges and faces of Eq. (3), respectively. Each vertex $\boldsymbol{r}_j$ is connected to six edges, with the exception of the 12 original vertices of the icosahedron that are connected to only five edges (see Fig. 11). Thus, each of the sums in Eq. (B.1) will contain only five or six terms for a given coordinate j.

First consider the partial derivatives of the radial gravity that are related to changes in the geometry of the edges. For a single edge that is connected by vertices $\boldsymbol{r}_j$ and $\boldsymbol{r}_2$, two triangular faces $(\boldsymbol{r}_j, \boldsymbol{r}_2, \boldsymbol{r}_3)$ and $(\boldsymbol{r}_j, \boldsymbol{r}_4, \boldsymbol{r}_2)$ with unit normal vectors $\hat{\boldsymbol{n}}_A$ and $\hat{\boldsymbol{n}}_B$, respectively, are connected to this edge. By using Eq. (3), the derivative with respect to r_j for this edge can be shown to be

$$\begin{aligned}
\frac{\partial g_i^E}{\partial r_j} = G\rho \Bigg[&\left\{ \frac{\partial \hat{\boldsymbol{n}}_A}{\partial r_j} \left(\hat{\boldsymbol{n}}_{j2}^A \cdot \boldsymbol{r}_e \right) + \hat{\boldsymbol{n}}_A \left(\frac{\partial \hat{\boldsymbol{n}}_{j2}^A}{\partial r_j} \cdot \boldsymbol{r}_e \right) \right. \\
&+ \hat{\boldsymbol{n}}_A \left(\hat{\boldsymbol{n}}_{j2}^A \cdot \frac{\partial \boldsymbol{r}_e}{\partial r_j} \right) + \frac{\partial \hat{\boldsymbol{n}}_B}{\partial r_j} \left(\hat{\boldsymbol{n}}_{2j}^B \cdot \boldsymbol{r}_e \right) \\
&+ \hat{\boldsymbol{n}}_B \left(\frac{\partial \hat{\boldsymbol{n}}_{2j}^B}{\partial r_j} \cdot \boldsymbol{r}_e \right) + \left. \hat{\boldsymbol{n}}_B \left(\hat{\boldsymbol{n}}_{2j}^B \cdot \frac{\partial \boldsymbol{r}_e}{\partial r_j} \right) \right\} L_e \\
&+ \left\{ \hat{\boldsymbol{n}}_A \left(\hat{\boldsymbol{n}}_{j2}^A \cdot \boldsymbol{r}_e \right) + \hat{\boldsymbol{n}}_B \left(\hat{\boldsymbol{n}}_{2j}^B \cdot \boldsymbol{r}_e \right) \right\} \frac{\partial L_e}{\partial r_j} \Bigg]. \tag{B.2}
\end{aligned}$$

In calculating the derivatives of the unit vectors, consider an arbitrary vector $\boldsymbol{n}$: the partial derivative of its corresponding unit vector with respect to r_j is

$$\frac{\partial \hat{\boldsymbol{n}}}{\partial r_j} = \frac{1}{|\boldsymbol{n}|}\left(\frac{\partial \boldsymbol{n}}{\partial r_j} - \hat{\boldsymbol{n}}\frac{\partial |\boldsymbol{n}|}{\partial r_j} \right), \tag{B.3}$$

where

$$\frac{\partial |\boldsymbol{n}|}{\partial r_j} = \frac{1}{|\boldsymbol{n}|}\left(\boldsymbol{n} \cdot \frac{\partial \boldsymbol{n}}{\partial r_j} \right). \tag{B.4}$$

For the case where the vector $\boldsymbol{n}$ is given by

$$\boldsymbol{n}_A = (\boldsymbol{r}_2 - \boldsymbol{r}_j) \times (\boldsymbol{r}_3 - \boldsymbol{r}_j), \tag{B.5}$$

$$\boldsymbol{n}_B = (\boldsymbol{r}_4 - \boldsymbol{r}_j) \times (\boldsymbol{r}_2 - \boldsymbol{r}_j), \tag{B.6}$$

$$\boldsymbol{n}_{j2}^A = (\boldsymbol{r}_2 - \boldsymbol{r}_j) \times \boldsymbol{n}_A, \tag{B.7}$$

$$\boldsymbol{n}_{2j}^B = (\boldsymbol{r}_j - \boldsymbol{r}_2) \times \boldsymbol{n}_B, \tag{B.8}$$

we have

$$\frac{\partial \boldsymbol{n}_A}{\partial r_j} = \frac{\boldsymbol{r}_j \times (\boldsymbol{r}_2 - \boldsymbol{r}_3)}{r_j}, \tag{B.9}$$

$$\frac{\partial \boldsymbol{n}_B}{\partial r_j} = \frac{\boldsymbol{r}_j \times (\boldsymbol{r}_4 - \boldsymbol{r}_2)}{r_j}, \tag{B.10}$$

$$\frac{\partial \boldsymbol{n}_{j2}^A}{\partial r_j} = (\boldsymbol{r}_2 - \boldsymbol{r}_j) \times \frac{\partial \boldsymbol{n}_A}{\partial r_j} - \frac{\boldsymbol{r}_j \times \boldsymbol{n}_A}{r_j}, \tag{B.11}$$

$$\frac{\partial \boldsymbol{n}_{2j}^B}{\partial r_j} = (\boldsymbol{r}_j - \boldsymbol{r}_2) \times \frac{\partial \boldsymbol{n}_B}{\partial r_j} + \frac{\boldsymbol{r}_j \times \boldsymbol{n}_B}{r_j}, \tag{B.12}$$

for the required derivatives in Eqs. (B.3) and (B.4). Furthermore, we have

$$\frac{\partial \boldsymbol{r}_e}{\partial r_j} = \frac{\boldsymbol{r}_j}{r_j} \tag{B.13}$$

and finally

$$\frac{\partial L_e}{\partial r_j} = \frac{1}{a+b+e}\frac{\partial (a+e)}{\partial r_j} - \frac{1}{a+b-e}\frac{\partial (a-e)}{\partial r_j}, \tag{B.14}$$

where

$$\frac{\partial a}{\partial r_j} = \frac{\boldsymbol{r}_j \cdot (\boldsymbol{r}_j - \boldsymbol{r})}{a r_j} \tag{B.15}$$

and

$$\frac{\partial e}{\partial r_j} = \frac{\boldsymbol{r}_j \cdot (\boldsymbol{r}_j - \boldsymbol{r}_2)}{e r_j}. \tag{B.16}$$

Next consider the partial derivatives of the radial gravity that are related to changes in the geometry of the faces. Consider first only a single face, whose vertices are given by $\boldsymbol{r}_j$, $\boldsymbol{r}_2$, and $\boldsymbol{r}_3$, and that are ordered counter clockwise about the face normal $\hat{\boldsymbol{n}}_f$. By using Eq. (3), the derivative with respect to r_j for this face can be shown to be

$$\begin{aligned}
\frac{\partial g_i^F}{\partial r_j} = -G\rho\Bigg[& \frac{\partial \hat{\boldsymbol{n}}_f}{\partial r_j}(\hat{\boldsymbol{n}}_f \cdot \boldsymbol{r}_f)\omega_f + \hat{\boldsymbol{n}}_f\left(\frac{\partial \hat{\boldsymbol{n}}_f}{\partial r_j} \cdot \boldsymbol{r}_f \right)\omega_f \\
& + \hat{\boldsymbol{n}}_f\left(\hat{\boldsymbol{n}}_f \cdot \frac{\partial \boldsymbol{r}_f}{\partial r_j} \right)\omega_f + \hat{\boldsymbol{n}}_f(\hat{\boldsymbol{n}}_f \cdot \boldsymbol{r}_f)\frac{\partial \omega_f}{\partial r_j} \Bigg],
\end{aligned} \tag{B.17}$$

where $\boldsymbol{r}_f$ is the vector from the observation point $\boldsymbol{r}$ to vertex $\boldsymbol{r}_j$. The partial derivatives of $\hat{\boldsymbol{n}}_f$ and $\boldsymbol{r}_f$ are equivalent to those in Eqs. (B.3)–(B.5), (B.9) and (B.13), and the partial derivative of ω_f with respect to r_j is

$$\frac{\partial \omega_f}{\partial r_j} = \frac{2\alpha}{\alpha^2 + \beta^2}\left(\frac{\partial \beta}{\partial r_j} - \frac{\beta}{\alpha}\frac{\partial \alpha}{\partial r_j} \right), \tag{B.18}$$

where α and β are given by Eqs. (7) and (8), respectively, and

$$\begin{aligned}
\frac{\partial \alpha}{\partial r_j} = {} & \frac{\boldsymbol{r}_j \cdot (\boldsymbol{r}_j - \boldsymbol{r})}{r_j|\boldsymbol{r}_j - \boldsymbol{r}|}\big\{ |\boldsymbol{r}_2 - \boldsymbol{r}||\boldsymbol{r}_3 - \boldsymbol{r}| + (\boldsymbol{r}_2 - \boldsymbol{r}) \cdot (\boldsymbol{r}_3 - \boldsymbol{r}) \big\} \\
& + \big\{ |\boldsymbol{r}_2 - \boldsymbol{r}|(\boldsymbol{r}_3 - \boldsymbol{r}) + |\boldsymbol{r}_3 - \boldsymbol{r}|(\boldsymbol{r}_2 - \boldsymbol{r}) \big\} \cdot \frac{\boldsymbol{r}_j}{r_j},
\end{aligned} \tag{B.19}$$

$$\frac{\partial \beta}{\partial r_j} = \frac{\boldsymbol{r}_j}{r_j} \cdot (\boldsymbol{r}_2 - \boldsymbol{r}) \times (\boldsymbol{r}_3 - \boldsymbol{r}). \tag{B.20}$$

References

Archinal, B.A., Rosiek, M.R., Kirk, R.L., Redding, B.L., 2006. The unified lunar control network 2005. Open-File Report 2006-1367, v. 1.0.

Belleguic, V., Lognonné, P., Wieczorek, M., 2005. Constraints on the martian lithosphere from gravity and topography data. J. Geophys. Res. 110, doi:10.1029/2005JE002437. E11005.

Bratt, S.R., Solomon, S.C., Head, J.W., Thurber, C.H., 1985. The deep structure of lunar basins: Implications for basin formation and modification. J. Geophys. Res. 90, 3049–3064.

Campbell, B.A., Hawke, B.R., 2005. Radar mapping of lunar cryptomaria east of Orientale basin. J. Geophys. Res. 110. E09002.

Chenet, H., Lognonné, P., Wieczorek, M.A., Mizutani, H., 2006. Lateral variations of lunar crustal thickness from the Apollo seismic data set. Earth Planet. Sci. Lett. 243, 1–14.

Cook, A.C., Spudis, P.D., Robinson, M.S., Watters, T.R., 2002. Lunar topography and basins mapped using a Clementine stereo digital elevation model. Lunar Planet. Sci. 33. Abstract 1281.

Croft, S.K., 1980. Cratering flow fields: Implications for excavation and transient expansion stages of crater formation. Proc. Lunar Sci. Conf. 11, 2347–2378.

Dalrymple, G.B., Ryder, G., 1996. ^{40}Ar/^{39}Ar age spectra of Apollo 17 highlands breccia samples by laser step-heating and the age of the Serenitatis basin. J. Geophys. Res. 101, 26069–26084.

Gagnepain-Beyneix, J., Lognonné, P., Chenet, H., Spohn, T., Lombardi, D., 2006. Seismic models of the Moon and their constraints on the mantle temperature and mineralogy. Phys. Earth Planet. Int. 159, 140–166.

Goins, N., Dainty, A., Toksöz, N., 1981. Structure of the lunar crust at highland site Apollo station 16. Geophys. Res. Lett. 8, 29–32.

Halekas, J.S., Lin, R.P., Mitchell, D.L., 2003. Magnetic fields of lunar multiring impact basins. Meteorit. Planet. Sci. 38, 565–578.

Haskin, L.A., Korotev, R.L., Rockow, K.M., Jolliff, B.L., 1998. The case for an Imbrium origin of the Apollo Th-rich impact-melt breccias. Meteorit. Planet. Sci. 33, 959–975.

Hikida, H., Mizutani, H., 2005. Mass and moment of inertia constraints on the lunar crustal thickness: Relations between crustal density, mantle density, and the reference radius of the crust–mantle boundary. Earth Planets Space 57, 1121–1126.

Hood, L.L., Mitchell, D.L., Lin, R.P., Acuña, M.H., Binder, A.B., 1999. Initial measurements of the lunar induced magnetic dipole moment using Lunar Prospector magnetometer data. Geophys. Res. Lett. 26, 2327–2330.

Jolliff, B.L., Gillis, J.J., Haskin, L.A., Korotev, R.L., Wieczorek, M.A., 2000. Major lunar crustal terranes: Surface expressions and crust–mantle origins. J. Geophys. Res. 105 (E2), 4197–4216.

Kato, M., Takizawa, T., Sasaki, S., SELENE Project Team, 2007. The SELENE mission: Present status and science goals. Lunar Planet. Sci. 38. Abstract 1211.

Khan, A., Mosegaard, K., 2002. An inquiry into the lunar interior: A non-linear inversion of the Apollo lunar seismic data. J. Geophys. Res. 107 (E6). 3-1-3-23.

Khan, A., Mosegaard, K., 2005. Further constraints on the deep lunar interior. Geophys. Res. Let. 32 (22). L22203.

Khan, A., Mosegaard, K., Rasmussen, K.L., 2000. A new seismic velocity model for the Moon from a Monte Carlo inversion of the Apollo lunar seismic data. Geophys. Res. Lett. 27, 1591–1594.

Khan, A., Mosegaard, K., Williams, J.G., Lognonné, P., 2004. Does the Moon possess a molten core? Probing the deep lunar interior using results from LLR and Lunar Prospector. J. Geophys. Res. 109 (E9). E09007.

Khan, A., Maclennan, J., Taylor, S.R., Connolly, A.D., 2006. Are the Earth and the Moon compositionally alike? Inferences on lunar composition and implications for lunar origin and evolution from geophysical modeling. J. Geophys. Res. 111 (E5). E05005.

Konopliv, A.S., Binder, A.B., Hood, L.L., Kucinskas, A.B., Sjogren, W.L., Williams, J.C., 1998. Improved gravity field of the Moon from Lunar Prospector. Science 281, 1476–1480.

Konopliv, A.S., Asmar, S.W., Carranza, E., Sjogren, W.L., Yuan, D.N., 2001. Recent gravity models as a result of the Lunar Prospector mission. Icarus 150, 1–18.

Korotev, R.L., 2000. The great lunar hot spot and the composition and origin of the Apollo mafic ("LKFM") impact-melt breccias. J. Geophys. Res. 105, 4317–4346.

Korotev, R.L., Gillis, J.J., Haskin, L.A., Jolliff, B.J., 2002. On the age of the Nectaris basin. In: Workshop on Moon Beyond 2002. Abstract 3029.

Kuskov, O.L., Kronrod, V.A., Hood, L.L., 2002. Geochemical constraints on the seismic properties of the lunar mantle. Phys. Earth Planet. Int. 134, 175–189.

Lognonné, P., Johnson, C., 2007. Planetary seismology. Treatise Geophys. 10, in press.

Lognonné, P., Gagnepain-Beyneix, J., Chenet, H., 2003. A new seismic model of the Moon: Implication for structure, thermal evolution and formation of the Moon. Earth Planet. Sci. Lett. 211, 27–44.

Melosh, H.J., 1979. Acoustic fluidization: A new geologic process. J. Geophys. Res. 84, 7513–7520.

Melosh, H.J., 1989. Impact Cratering: A Geologic Process. Oxford Univ. Press, London, UK.

Milani, A., Rossi, A., Vokrouhlický, D., Villani, D., Bonanno, C., 2001. Gravity field and rotation state of Mercury from the BepiColombo radio science experiments. Planet. Space Sci. 49, 1579–1596.

Mohit, P.S., Phillips, R.J., 2006. Viscoelastic evolution of lunar multiring basins. J. Geophys. Res. 111, doi:10.1029/2005JE002654. E12001.

Muller, P.M., Sjogren, W.L., 1968. Mascons: Lunar mass concentrations. Science 161, 680–684.

Neumann, G.A., Zuber, M.T., Smith, D.E., Lemoine, F.G., 1996. The lunar crust: Global structure and signature of major basins. J. Geophys. Res. 101, 16841–16843.

Neumann, G.A., Zuber, M.T., Wieczorek, M.A., McGovern, P.J., Lemoine, F.G., Smith, D.E., 2004. Crustal structure of Mars from gravity and topography. J. Geophys. Res. 109. E08002.

O'Keefe, J.D., Ahrens, T.J., 1993. Planetary cratering mechanics. J. Geophys. Res. 98, 17011–17028.

Phillips, R.J., Dvorak, J., 1981. The origin of lunar mascons: Analysis of the Bouguer gravity associated with Grimaldi. In: Schultz, P.H., Merrill, R.B. (Eds.), Multiring Basins. Pergamon, pp. 91–104.

Phipps Morgan, J., Blackman, D.K., 1993. Inversion of combined gravity and bathymetry data for crustal structure: A prescription for downward continuation. Earth Planet. Sci. Lett. 119, 167–179.

Pieters, C.M., Tompkins, S., Head, J.W., Hess, P.C., 1997. Mineralogy of the mafic anomaly in the South Pole–Aitken Basin: Implications for excavation of the lunar mantle. Geophys. Res. Lett. 24, 1903–1906.

Pike, R.J., 1976. Crater dimensions from Apollo data and supplemental sources. Moon 15, 463–477.

Potts, L.V., von Frese, R.R.B., 2003a. Comprehensive mass modeling of the Moon from spectrally correlated free-air and terrain gravity data. J. Geophys. Res. 108 (E4), doi:10.1029/2000JE001440. 5024.

Potts, L.V., von Frese, R.R.B., 2003b. Crustal attributes of lunar basins from terrain-correlated free-air gravity anomalies. J. Geophys. Res. 108 (E5), doi:10.1029/2000JE001446. 5037.

Press, W.H., Teukolsky, S.A., Vetterling, W.T., Flanner, B.P., 1992. Numerical Recipes in FORTRAN: The Art of Scientific Computing. Cambridge Univ. Press, Cambridge, UK.

Righter, K., 2002. Does the Moon have a metallic core? Constraints from giant Impact modeling and siderophile elements. Icarus 158, 1–13.

Ryder, G., 1994. Coincidence in time of the Imbrium basin impact and the Apollo 15 volcanic flows: The case for impact induced melting. Geol. Soc. Am. Spec. Paper 293, 11–18.

Sadourny, R., Arakawa, A., Mintz, Y., 1968. Integration of the non-divergent barotropic vorticity equation with an icosahedal–hexagonal grid for the sphere. Mon. Weath. Rev. 96, 351–356.

Smith, W.H.F., Wessel, P., 1990. Gridding with continuous curvature splines in tension. Geophysics 55, 293–305.

Smith, D.E., Zuber, M.T., Neumann, G.A., Lemoine, F.G., 1997. Topography of the Moon from the Clementine lidar. J. Geophys. Res. 102, 1519–1611.

Solomon, S.C., Head, J.W., 1980. Lunar mascon basins: Lava filling, tectonics, and evolution of the lithosphere. Rev. Geophys. Space Phys. 18, 107–141.

Solomon, S.C., Longhi, J., 1977. Magma oceanography. 1. Thermal evolution. Proc. Lunar Sci. Conf. 8, 884–886.

Solomon, S.C., and 20 colleagues, 2001. The MESSENGER mission to Mercury: Scientific objectives and implementation. Planet. Space Sci. 49, 1445–1465.

Spudis, P.D., 1993. The Geology of Multiring Impact Basins. Cambridge Univ. Press, Cambridge, UK.

Toksöz, M.N., Dainty, A.M., Solomon, S.C., Anderson, K., 1974. Structure of the Moon. Rev. Geophys. Space Phys. 12, 539–567.

Tompkins, S., Pieters, C.M., 1999. Mineralogy of the lunar crust: Results from Clementine. Meteor. Planet. Sci. 34, 25–41.

Turcotte, D.L., Schubert, G., 1982. Geodynamics. Cambridge Univ. Press, Cambridge, UK.

US Geological Survey, 2002. Color-coded topography and shaded relief map of the lunar near side and far side hemispheres. I-2769.

von Frese, R.R.B., Tan, L., Potts, L.V., Kim, J.W., Merry, C.J., Bossler, J.D., 1997. Lunar crustal analysis of Mare Orientale from topographic and gravity correlations. J. Geophys. Res. 102 (E11), 25657–25676.

Werner, R.A., Scheeres, D.J., 1997. Exterior gravitation of a polyhedron derived and compared with harmonic and mascon gravitation representations of Asteroid 4769 Castalia. Celest. Mech. Dynam. Astron. 65, 313–344.

Wieczorek, M.A., 2007. Gravity and topography of the terrestrial planets. Treatise Geophys. 10, in press.

Wieczorek, M.A., Phillips, R.J., 1997. The structure and compensation of the lunar highland crust. J. Geophys. Res. 102, 10933–10943.

Wieczorek, M.A., Phillips, R.J., 1998. Potential anomalies on a sphere: Applications to the thickness of the lunar crust. J. Geophys. Res. 103, 1715–1724.

Wieczorek, M.A., Phillips, R.J., 1999. Lunar multiring basins and the cratering process. Icarus 139, 246–259.

Wieczorek, M.A., Phillips, R.J., 2000. The "Procellarum KREEP Terrane": Implications for mare volcanism and lunar evolution. J. Geophys. Res. 105, 20417–20430.

Wieczorek, M.A., Zuber, M.T., 2001. The composition and origin of the lunar crust: Constraints from central peaks and crustal thickness modeling. Geophys. Res. Lett. 28, 4023–4026.

Wieczorek, M.A., Jolliff, B.L., Khan, A., Pritchard, M.E., Weiss, B.P., Williams, J.G., Hood, L.L., Righter, K., Neal, C.R., Shearer, C.K., McCallum, I.S., Tompkins, S., Hawke, B.R., Peterson, C., Gillis, J.J., Bussey, B., 2006. The constitution and structure of the lunar interior. In: Jolliff, B.L., Wieczorek, M.A., Shearer, C.K., Neal, C.R. (Eds.), New Views of the Moon. Mineralogical Society of America, Chantilly, pp. 221–364.

Wilhelms, D.E., 1984. The Moon. In: Carr, M. (Ed.), The Geology of the Terrestrial Planets. NASA SP-469, pp. 107–205.

Wilhelms, D.E., 1987. The Geologic History of the Moon. US Geol. Surv. Prof. Pap. 1348. US Government Printing Office, Washington, DC.

Williams, J.G., Boggs, D.H., Yoder, C.F., Ratcliff, J.T., Dickey, J.O., 2001. Lunar rotational dissipation in solid body and molten core. J. Geophys. Res. 106, 27933–27968.

Williams, K.K., Zuber, M.T., 1998. Measurements and analysis of lunar basin deposits from Clementine altimetry. Icarus 131, 107–122.

Zuber, M.T., Smith, D.E., Lemoine, F.G., Neumann, G.A., 1994. The shape and internal structure of the Moon from Clementine mission. Science 266, 1839–1843.